Fully automatic segmentation of left ventricular anatomy in 3-D LGE-MRI

Tanja Kurzendorfer [a],[*], Christoph Forman [b], Michaela Schmidt [b], Christoph Tillmanns [c], Andreas Maier [a], Alexander Brost [d]

[a] Pattern Recognition Lab, Department of Computer Science, Friedrich-Alexander-University Erlangen-Nuremberg, Erlangen, Germany
[b] Siemens Healthcare GmbH, MR Predevelopment and Innovation, Erlangen, Germany
[c] Diagnostikum Berlin, Kardiologie, Berlin, Germany
[d] Siemens Healthcare GmbH, Advanced Therapies, Forchheim, Germany

ARTICLE INFO

ABSTRACT

The current challenge for electrophysiology procedures, targeting the left ventricle, is the localization and qualification of myocardial scar. Late gadolinium enhanced magnetic resonance imaging (LGE-MRI) is the current gold standard to visualize regions of myocardial infarction. Commonly, a stack of 2-D images is acquired of the left ventricle in short-axis orientation. Recently, 3-D LGE-MRI methods were proposed that continuously cover the whole heart with a high resolution within a single acquisition. The acquisition promises an accurate quantification of the myocardium to the extent of myocardial scarring. The major challenge arises in the analysis of the resulting images, as the accurate segmentation of the myocardium is a requirement for a precise scar tissue quantification. In this work, we propose a novel approach for fully automatic left ventricle segmentation in 3-D whole-heart LGE-MRI, to address this limitation. First, a two-step registration is performed to initialize the left ventricle. In the next step, the principal components are computed and a pseudo short axis view of the left ventricle is estimated. The refinement of the endocardium and epicardium is performed in polar space. Prior knowledge for shape and inter-slice smoothness is used during segmentation. The proposed method was evaluated on 30 clinical 3-D LGE-MRI datasets from individual patients obtained at two different clinical sites and were compared to gold standard segmentations of two clinical experts. This comparison resulted in a Dice coefficient of 0.83 for the endocardium and 0.80 for the epicardium.

© 2017 Elsevier Ltd. All rights reserved.

1. Introduction

About 26 million people worldwide are suffering from heart failure (HF) (Ponikowski et al., 2014). The symptoms of HF typically include shortness of breath, signs of fluid retention, fatigue, exercise intolerance, and depression (Shea and Sweeney, 2003). The underlying cardiac cause of HF is most often a myocardial infarction (McMurray et al., 2012). According to Dickstein et al. (2009) at least 51% of patients suffering from HF have an ischemic history.

The viability assessment of the myocardium after a myocardial infarction is very important for diagnosis, therapy planning, success prediction of the therapy, and patient prognosis. Especially, the location and quantification of a patient's scar burden promises to increase the success rate of different therapies, such as ablation

of ventricular tachycardia or cardiac resynchronization therapy (Dikici et al., 2004; Karim et al., 2013). Late gadolinium enhanced magnetic resonance imaging (LGE-MRI) is the clinical gold standard for non-invasive assessment of myocardial viability (Börnert and Jensen, 1995; Kellman and Arai, 2012; Rashid et al., 2015; Shin et al., 2014). The LGE images are acquired around 10–20 min after contrast agent injection. LGE-MRI uses the difference in contrast agent accumulation between viable and damaged tissue. In clinical routine, 2-D short axis (SA) slices along the left ventricle (LV) are acquired, with a large slice thickness in the range of 5–10 mm (Ciofolo and Fradkin, 2008). See Fig. 1(a) and (b) for an example of a 2-D SA LGE-MRI data set.

Recently, LGE-MRI was extended to 3-D, to continuously cover the whole heart with a high resolution of up to $(0.7 \times 0.7 \times 1.5)\,\text{mm}^3$ in a single acquisition. This scan promises an accurate quantification of the myocardium to the extent of myocardial infarction (Shin et al., 2014), see Fig. 1(c) and (d) for an example. The 3-D LGE-MRI sequence is currently in medical research, nonetheless it has the

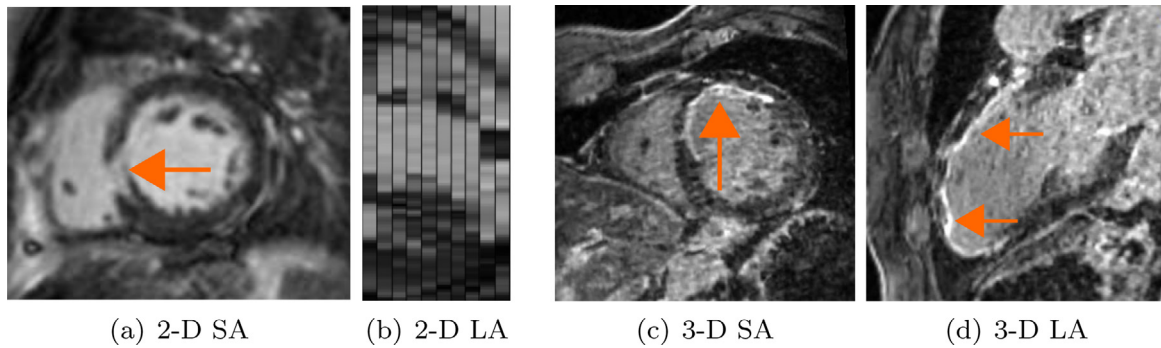(a) 2-D SA   (b) 2-D LA   (c) 3-D SA   (d) 3-D LA

Fig. 1. (a) 2-D late gadolinium enhanced short axis slice of the left ventricle, with a myocardial infarction (orange arrow). (b) Long axis view of the 2-D SA data, with a bad inter-slice resolution because of the large slice thickness and distance between the slices. The 2-D LGE-MRI sequence has the following parameters: pixel spacing $(1.77 \times 1.77)\,mm^2$, slice thickness 8 mm, spacing between the slices 10 mm, number of slices 10. (c) 3-D LGE-MRI reorientated in a pseudo short axis view. (d) 3-D LGE-MRI in a pseudo long axis view. With the 3-D LGE-MRI an accurate quantification to the extent of myocardial scarring is possible, the orange arrows are pointing to the MI. The 3-D LGE-MRI sequence has the following parameters: pixel spacing $(1.30 \times 1.30)\,mm^2$, slice thickness 1.30 mm, number of slices 120. (For interpretation of the references to color in this figure legend, the reader is referred to the web version of this article.)

potential to become clinical routine, because of the detailed visualization of MI. Besides the technological improvements regarding image acquisition and the clear clinical demand (Bilchick et al., 2008), the challenge arises in providing automatic tools for fast image analysis.

In clinical routine, manual outlining of the left ventricle's myocardium is commonly the standard for performing the LV segmentation. However, such a segmentation is tedious, time consuming, prone to user errors, and intra- and inter-observer variability (Frangi et al., 2001). Considering the 3-D LGE-MRI data, one would have to annotate about 80 slices to cover the left ventricle. The amount of annotations renders methods, based solely on manual interaction impractical. However, most scar quantification algorithms require an accurate segmentation of the LV myocardium.

The main issue with processing LGE-MRI data is the non-homogeneous intensity distribution within the myocardium, resulting from the different accumulations of contrast agent in the damaged tissue. Therefore, often the CINE MRI is segmented and the contours are registered to the LGE-MRI. The registration and fitting from the CINE MRI to the LGE-MRI has several problems. The global position of the heart may change during the acquisitions due to patient movement. The cardiac phases from the CINE MRI may not precisely match to the LGE-MRI. Inter-slice shifts can arise from multiple breath-holds. Even though these shifts may appear minor, they can lead to significant errors in the myocardial scar quantification.

Moreover, the 3-D whole heart acquisition does not allow a direct use of any ring or circular shape prior, as commonly used for 2-D SA images. To overcome these issues, we propose a novel approach for fully automatic left ventricle segmentation using solely 3-D LGE-MRI data. The novelty of the method lies in the combination of an edge array and a scar exclusion step, to initialize a minimal cost path search in polar space. Furthermore, no anatomical scan is required for the segmentation and no user interaction.

2. Previous work

The delineation of the myocardium is a prerequisite for automatic scar quantification (Karim et al., 2016). Segmentation methods to extract the endocard and epicard of the left ventricle using 2-D SA acquisitions most often rely on the registration of the LGE-MRI to an anatomical MRI scan (Ciofolo et al., 2008; Dikici et al., 2004; Tao et al., 2015; Wei et al., 2011) or shape priors (Albà et al., 2014). CINE MRI scans have an uniform texture and the wall delineation is more visible compared to LGE-MRI, therefore,

the segmentation of CINE MRI has been well studied in literature (Petitjean and Dacher, 2011; Suinesiaputra et al., 2014). However, little research has been done for fully automatic myocardium segmentation using solely LGE-MRI.

Dikici et al. (2004) uses a non-rigid variational approach to register the CINE MRI with the LGE-MRI. Afterwards, active contours are used to optimize a parametric affine transform of the propagated parameters. Ciofolo et al. (2008) proposed to deform a geometrical template to fit to the myocardial contour for each MRI slice. In addition, the LV was divided into four quadrants and those likely to contain large areas of myocardial scarring were treated differently. The contours from the CINE MRI were then aligned to the geometrical template of the LGE-MRI. Wei et al. (2011) uses a model based approach for the LV segmentation that comprises several steps. Inter-slice shifts in CINE MRI images are corrected and the LGE-MRI is registered to the CINE MRI. The CINE MRI contours are further deformed by features in the LGE short or long axis images. Tao et al. (2015) proposes a four step algorithm to segment the LV from LGE-MRI. The LGE-MRI is aligned to the CINE MRI. The endo- and epicardial borders from CINE MRI are fitted to the LGE-MRI, optimized in 3-D and refined based on the LGE-MRI.

Albà et al. (2014) proposed a modified graph cut approach to segment the LV using 2-D LGE-MRI. Therefore, six rules were defined: (i) the blood pool appears bright, (ii) the blood pool has a circular shape, (iii) the blood pool is continuous in the longitudinal direction, (iv) the myocardium can include dark and bright voxels, (v) the myocardial thickness changes smoothly, and (vi) the 3-D global shape of the myocardium is smooth. The method from Albà et al. does not use information from CINE MRI. The direct segmentation using LGE-MRI avoids segmentation errors caused by the use of the 2-D CINE MRI and a misalignment between the sequences. In addition, it allows for a faster segmentation approach. Hence, the direct segmentation based solely on LGE-MRI is desirable. All the presented methods use 2-D SA LGE-MRI scans.

To the best of our knowledge, there has been little research aimed using 3-D LGE-MRI images. The first semi-automatic solution for myocardial segmentation using solely 3-D LGE-MRI was proposed by Kurzendorfer et al. (2015). The segmentation comprises three steps. First, an initial seed-point within the LV cavity had to be selected by the user. An approximation of the endocardium was achieved using morphological active contours without edges. The SA view was estimated using principal component analysis. Next the endo- and epicardial contours were refined in polar space using edge information.

Our work is distinct from the aforementioned, also when compared to Kurzendorfer et al. (2015), in several aspects. First, the
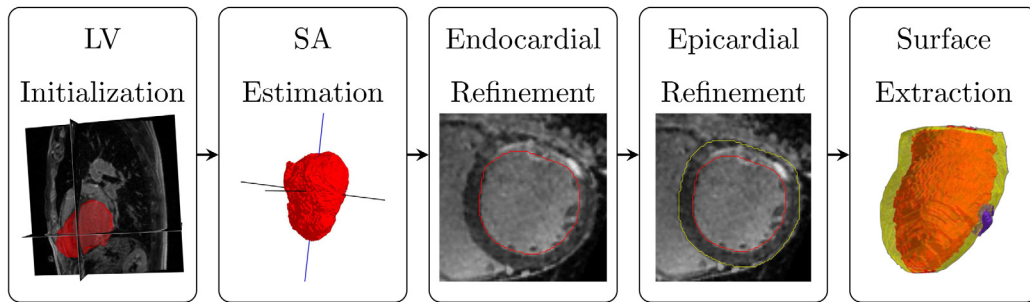
Fig. 2. Overview of the segmentation pipeline. First, the left ventricle is initialized using a registration based approach. In the next step, the short axis view is estimated with the help of principal component analysis. In the third step, the endocardial contour is refined in polar space. In the fourth step, the epicard is extracted. In the final step, the contours can be exported as surface meshes and used for further processing.

method is fully automatic, where the initial seed-point and the active contours segmentation is replaced by a two-step registration approach. Furthermore, prior knowledge, in terms of constraints for shape and inter-slice smoothness is used for the myocardial segmentation. And solely the 3-D whole heart LGE-MRI data set is used for the segmentation.

3. Methods

Our approach comprises of five steps: First, a two-step registration is performed for an initialization of the LV. Second, the principal axes of the LV are computed and a pseudo SA view is estimated. The endocardium is refined in polar space considering the edge and scar information and applying a minimal cost path search along the cost array. Fourth, the epicardium is estimated, starting from the endocardium and considering the edge information. Prior knowledge, such as shape and inter-slice smoothness constraints, is used during the refinement step. Finally, the endocardial and epicardial contours are exported as 3-D surface meshes using the marching cubes algorithm. Fig. 2 provides an overview of the segmentation pipeline.

3.1. Registration

For the initialization of the left ventricle within the 3-D whole heart scan, a two-stage registration to an atlas volume **A** is performed (Unberath et al., 2015). The segmentation of the atlas volume **A** was done manually, resulting in a labeled mask **L**. First, a multi resolution rigid registration is performed to roughly align the atlas volume **A** to the input volume **I**, see Fig. 3(b) for the registration result. The transformation **T** can be decomposed into scaling, rotation and translation. However, regarding cardiac image regis-

tration, more variations need to be allowed, to match the complex deformations and anatomical changes between different patients. Therefore, a non-rigid multi resolution registration is performed, the result is depicted in Fig. 3(c). Nevertheless, a rigid transform has to be applied prior to the non-rigid registration for an initialization, as non-rigid transformation most often cannot handle large scaling, translation or rotation.

The matching of the transformation is depending on the similarity measure. A mutual information based similarity measure is employed, where the image intensities are understood as random variables with a certain probability density function (Thévenaz et al., 2008). A random coordinate sampler is used, which is not limited to voxel positions. During the registration a linear interpolation is utilized. Regarding the non-rigid transformation, B-splines are applied for the parameterization to describe the local deformation of the left ventricle (Rueckert et al., 1999). B-splines are locally controlled which makes them computationally efficient even for larger number of control points. The spacing of the control points defines how local or global the non-rigid registration will be. Therefore, the proposed approach from Rueckert et al. (1999) was applied, using a hierarchical multi-resolution approach, were the number of control points vary according to the scale-space pyramid.

In the last step, the transformation of the two-stage registration is applied to the labeled mask **L** of the atlas volume **A**, resulting in a registered mask **M** (Klein et al., 2010).

3.2. Short axis estimation

After the initialization of the left ventricle through the two-stage registration approach, the short axis view of the left ventricle can be estimated using principal component analysis of the transformed atlas mask **M** (Jolliffe, 2002). The contour points of the mask **M**

(a) No registration   (b) Rigid registration   (c) Non-rigid registration
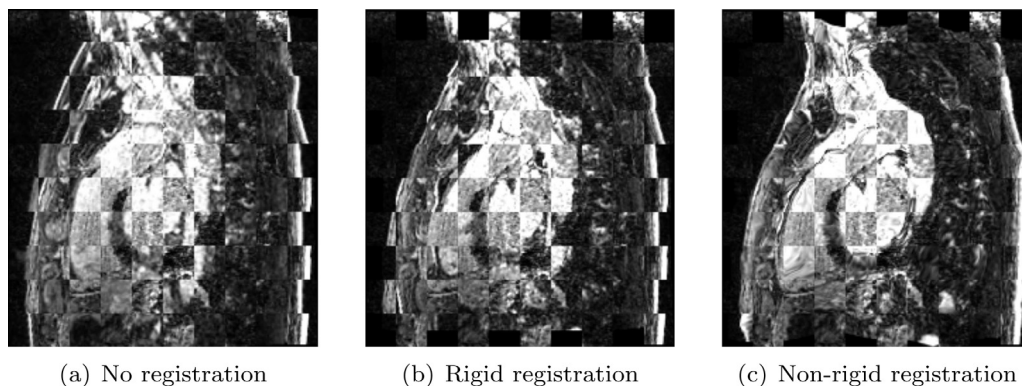
Fig. 3. (a) Checkerboard image before the registration, showing the thorax in a sagittal viewing plane. (b) Checkerboard image showing the registration result after the rigid registration. (c) Final result after the non-rigid registration.
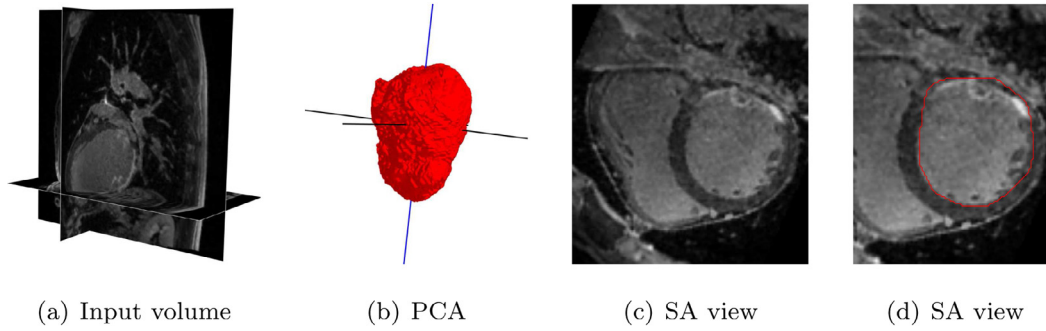
(a) Input volume   (b) PCA   (c) SA view   (d) SA view

Fig. 4. (a) 3-D LGE-MRI of the three orthogonal imaging planes, sagittal, coronal and axial. (b) Approximated cavity of the LV through the registration to the atlas data. The principal components are visualized, with the first principal component in blue and the second and third principal components in black. (c) Cropped pseudo short axis view after the principal component analysis. (d) Short axis view with the contour of the transformed mask in red. (For interpretation of the references to color in this figure legend, the reader is referred to the web version of this article.)

are extracted using the marching cubes algorithm (Lorensen and Cline, 1987), resulting in a set of vertices $\mathbf{v} \in \mathbb{R}^{N \times 3}$, where N is the number of vertices. The covariance matrix $\mathbf{\Sigma}$ is calculated, with $\mathbf{\Sigma} = \frac{1}{N-1} \sum_{i=1}^{N} (\mathbf{v}_i - \bar{\mathbf{v}})$, where $\bar{\mathbf{v}}$ is the mean vector of all vertices $\mathbf{v}$. Having the covariance matrix $\mathbf{\Sigma}$, the singular value decomposition is applied, which results in $\mathbf{\Sigma} = \mathbf{U}\mathbf{S}\mathbf{V}^T$. $\mathbf{U}$ is a 3×3 matrix, where the columns are orthogonal unit vectors. The first column corresponds to the largest eigenvalue and has the largest variation among the transformed mask, i.e. the short axis orientation. In the next step, the offset to the rotation center is calculated. Then, the affine transformation is applied to the volume $\mathbf{I}$ and the mask $\mathbf{M}$, to align the coordinate axis with the unit vectors of $\mathbf{U}$. See Fig. 4(b) for an illustration, with the first principal component marked in blue. The short axis view is commonly used for most segmentation approaches reported in literature, as most algorithms rely on standard 2-D LGE SA acquisitions. Having the short axis view, prior knowledge such as circularity and convexity of the contour points can be taken into account for the segmentation.

3.3. Endocardial contour extraction

As the rough outline of the left ventricle is known, the rotated volume $\mathbf{I}$ and the rotated mask $\mathbf{M}$ can be cropped around the region of interest and the further image processing steps are just performed on the cropped volume. The cropping of the volumes is done for computational efficiency. After a pseudo short axis view of the LV is estimated, the algorithm starts with the slice that corresponds to the center of mass of the transformed mask $\mathbf{M}$. The contour points $\mathbf{C} \in \mathbb{R}^{N \times 3}$ of the transformed atlas mask $\mathbf{M}$ are extracted using the marching cubes algorithm (Lorensen and Cline, 1987), where N is the number of newly extracted vertices in short axis orientation. Fig. 4(d) depicts the slice, that corresponds to the center of mass with the contour of the transformed mask $\mathbf{M}$ in red.

In the next step, the polar image is calculated, where the origin of the polar image corresponds to the center of the found contours $\mathbf{C}$, i.e. the center of mass. The polar space is useful for several reasons, the contours that we are looking for, has a roughly circular shape, therefore, all the contours in polar space have the same length, no matter which radius. Moreover, the image size is smaller, which allows for a faster processing. Fig. 4(c) shows the SA slice that corresponds to the center of mass with the extracted contours $\mathbf{C}_s$ of the marching cubes algorithm, where s is the current slice index. For the particular slice s, Fig. 5(a) is the analogue image in polar space. Through this mapping the Cartesian image coordinates (x, y) are converted to polar coordinates (r, ρ). The maximum radius r is selected to cover all potential myocardium boundaries and $\rho \in [0°, 360°]$. The contours $\mathbf{C}_s$ from the transformed mask are converted

to polar coordinates and used to refine the boundaries of the endocardium.

The edge information of the polar image is extracted by applying the Canny edge detection (Canny, 1986). To extract minor edges, a Gaussian smoothing with a standard deviation of $\sigma = 2.5$ is applied. The lower bound of the hysteresis thresholding was set to 10% of the maximum and the upper bound to 20%. The result is depicted in Fig. 5(b). In addition, the mean intensity of the blood pool μ_{bp} and the standard deviation σ_{bp} are estimated. Having these values, a scar threshold θ_{st} can be defined as $\theta_{st} = \mu_{bp} + \sigma_{bp}$. In the next step, all the pixels above this threshold are defined as potential scar candidates. Having the scar candidates all pixels with increasing radius are labeled with 1, resulting in a scar map, see Fig. 5(c). The scar map is then logically combined with the edge image, which derives the cost array $\mathbf{P}$ for the minimal cost path (MCP) search, as depicted in Fig. 5(d). Six equally distributed points are selected from the contour $\mathbf{C}_s$ and a MCP search algorithm is used to find the optimal contour (Dijkstra, 1959). The number of initialization points for the MCP was chosen heuristically. The MCP finds the distance weighted minimal cost path through the cost array $\mathbf{P}$. The cost path is simply calculated as the sum of the costs for each move of the path. Where edge pixels have 0 costs and non-edge and scar pixels 1. The cost of one step from point $\mathbf{p}_i$ to $\mathbf{p}_j$ is calculated as follows:

$$c(\mathbf{p}_i, \mathbf{p}_j) = \frac{d}{2} * \mathbf{P}(\mathbf{p}_i) + \frac{d}{2} * \mathbf{P}(\mathbf{p}_j), \tag{1}$$

where d is the distance between the two points $\mathbf{p}_i$ and $\mathbf{p}_j$, which are two neighboring points in the cost array $\mathbf{P}$. The diagonal versus horizontal or vertical steps are of different length and therefore, the path costs are weighted accordingly. The result of the MCP is visualized in Fig. 5(e) and (f). After the refinement, the contours $\mathbf{C}_s$ are converted back to Cartesian coordinates, as illustrated in Fig. 6(a). As the result is frayed and papillary muscles close to the endocardial border may be included, the convex hull is calculated for the estimated points. This assumption is based on the fact that the left ventricle's cavity is convex. The final endocardial contour $\mathbf{C}_f \in \mathbb{R}^{N_s \times 2}$ is derived from the smallest convex polygon, as shown in Fig. 6(b). After the first contour $\mathbf{C}_f$ is refined, the result is used for further improvement of the silhouettes in the lower and upper pseudo SA slices till the base and apex is reached. The refinement is performed in polar space as previously described. The distance between the previously found contour $\mathbf{C}_f$ and the silhouette from the transformed atlas mask $\mathbf{C}_s \in \mathbb{R}^{N_s \times 2}$ is calculated. If the distance

(a) Polar image with transformed mask in polar coordinates (red).

(b) Edge image using Canny.

(c) Scar map.

(d) Cost array for minimal cost path (MCP) search.

(e) Cost array with the found contour from MCP.

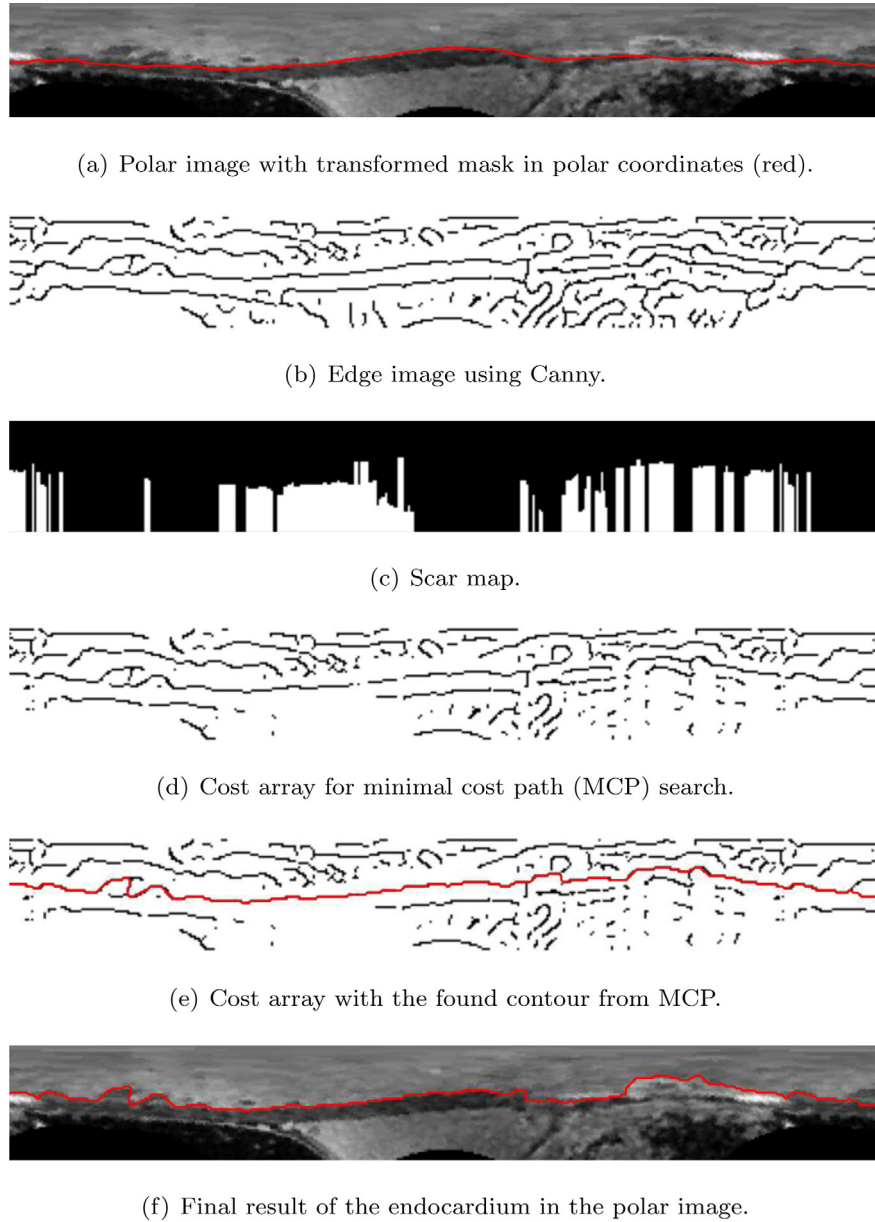(f) Final result of the endocardium in the polar image.

Fig. 5. Endocardial contour refinement in polar space. (a) Input image after polar transformation and the contour points in polar coordinates (red). (b) Edge information from Canny edge detector with a Gaussian smoothing of $\sigma = 2.5$. (c) Scar map. (d) Cost array for the minimal cost path search, combining the scar map and the Canny edge image. (e) Cost array with the found contour from the minimal cost path search. (d) Final result of the MCP in the polar image. (For interpretation of the references to color in this figure legend, the reader is referred to the web version of this article.)

is larger than a margin θ_{dist} the contour point of the transformed mask is not considered for the further improvement,

$$\mathbf{C}'^j_s = \begin{cases} \mathbf{C}^j_s & \text{if } \mathbf{C}^j_f - \mathbf{C}^j_s < \theta_{\text{dist}} \\ \{\} & \text{otherwise,} \end{cases} \qquad (2)$$

where j denotes the jth contour point and C'_s the updated contour of C_s. In the next step, the contour points $\mathbf{C}_f$ and $\mathbf{C}'_s$ are merged, $\mathbf{C}_m = \mathbf{C}_f \cup \mathbf{C}'_s$ and afterwards sub-sampled with a sampling rate of $\xi = 4$. The sub-sampling is performed in order to obtain a smoother contour and to remove single outliers. Afterwards, additional refinement steps for the endocardial contour $\mathbf{C}_m$ approximation are performed. The polar image is extended to the left ($\rho < 0°$) and right ($\rho > 360°$) with $\gamma \in [30°, 60°, 90°]$. From these enlarged polar images, the edge information is extracted, using the Canny edge detector, with a Gaussian smoothing of $\sigma = 3$, to extract

more dominant edges. The Gaussian smoothing of σ was chosen heuristically. Furthermore, the scar map is calculated, by applying θ_{st}. The cost array is derived from the scar map and the edge image. In addition, the sub-sampled silhouette points $\mathbf{C}_m$ are extended to the left and the right with the corresponding γ. The enlargement of the polar image is done, to avoid errors at the border of the edge image, in particular if papillary muscles or myocardial infarctions are present. As before, six equally distributed points are selected from the extended contours $\mathbf{C}_m$ for the initialization of the minimal cost path search, for all three cases with respect to γ. First, the shortest path for each of the three cases is chosen. Second, the length of the path is normalized with respect to the corresponding enlargement γ. The final contour $\mathbf{C}_f$ is selected from the results by choosing the solution with the minimal costs. This outline is then transferred back to Cartesian coordinates. The convex hull is computed for the refined points $\mathbf{C}_f$.
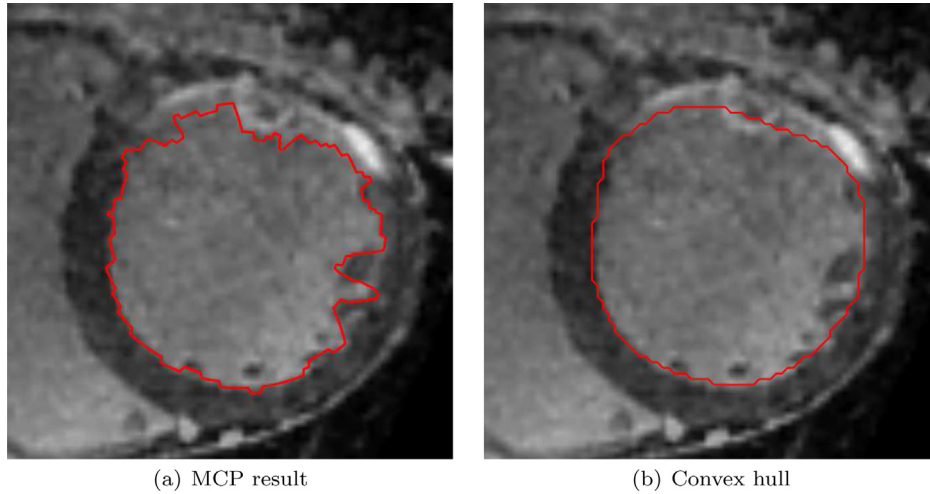
(a) MCP result (b) Convex hull

Fig. 6. Final steps of endocardial refinement. (a) Contour points after conversion from polar to Cartesian coordinates. (b) Convex hull of the endocardial outline in (a).

A round shape of the left ventricle in short axis view is assumed (Azancot et al., 1983; Duann et al., 1999; McLeod et al., 2015). For the inter-slice smoothness criteria, the shape of the previous contour to the newly found contour is compared. If the difference of the two contours is bigger than a certain margin θ_{diff}, the previous contour will be considered. Depending on the apical or basal direction, erosion is applied to the contour, as the convex hull slightly enlarges the contour, and in apical direction the radius is decreasing. For further improvements different constraints are considered depending on the apical or basal direction.

For the apical direction the center $\mathbf{c}_{\mathrm{pre}}$ of the final contour and the radius r_{pre} of the semi-axis from the previous slice are examined. As a high resolution is given through the 3-D acquisition technique, the center of the new curve $\mathbf{c}_{\mathrm{new}}$ has to be within a certain distance θ_{C} to the center of the previous curve $\mathbf{c}_{\mathrm{pre}}$. To be precise, a shift between two pseudo SA slices is not possible as they are computed from the same 3-D volume. Furthermore, the radius r_{new} should always be equal or smaller to the radius r_{pre} from the previous refined slice for the apical direction. If one of these constraints is not met, the previous contour is taken and erosion is applied, to achieve a slightly smaller radius

$$\mathbf{C}_{\mathrm{f}} = \begin{cases} \mathbf{C}_f & \text{if } \mathbf{c}_{\mathrm{pre}} - \mathbf{c}_{\mathrm{new}} < \theta_{\mathrm{C}} \cup r_{\mathrm{new}} \le r_{\mathrm{pre}} \\ E(\mathbf{C}_{pre}) & \text{otherwise,} \end{cases} \quad (3)$$

where E denotes the erosion. The apical iteration ends if the radius r_{new} of the semi-axis falls below a threshold θ_{r}. See Fig. 7(b) for an illustration of the apical refinement direction.

Similar conditions apply for the basal direction. Here, the center $\mathbf{c}_{\mathrm{new}}$ of the new curve and the center $\mathbf{c}_{\mathrm{pre}}$ of the curve from the previous slice and the previous contour shape are considered as well. If the distance between the centers is greater than a threshold θ_{C}, the endocardial contour is approximated as follows,

$$\mathbf{C}_{\mathrm{f}} = \begin{cases} \mathbf{C}_f & \text{if } \mathbf{c}_{\mathrm{pre}} - \mathbf{c}_{\mathrm{new}} < \theta_{\mathrm{C}} \\ \mathbf{C}_{pre} & \text{otherwise.} \end{cases} \quad (4)$$

The basal iteration either stops if the maximum point from the transformed mask is reached or the difference of the areas of the previous contour C_{pre} and the newly found contour C_{f} is greater than a threshold $\theta_{b_{\max}}$. In this case, the outflow tract is reached. See Fig. 7(a) for an illustration of the basal refinement direction.

3.4. Epicardial contour extraction

For the epicardial contour extraction the previously found endocardial points are used. The contour extraction is performed in polar space for the same reason as mentioned for the endocardial refinement. The edge information is extracted, using the Canny edge detector (Canny, 1986). The standard deviation σ of the Gaussian filter kernel is set to $\sigma = 2$, where σ was chosen heuristically. As the epicardium has to be greater then the endocardium, the radius is enlarged by θ_{epi}, as depicted in Fig. 8(a). In addition, all edges that fall within the endocardium are erased, see Fig. 8(b). Having the enlarged endocardial contour, the closest edge with increased radius is searched for in the Canny edge image. A polynomial is fitted through the found points to remove outliers. In the next step, the extracted contour points are transformed back to Cartesian coordinates. As the result might be frayed, the convex hull is estimated to smooth the contour. Due to the smoothing operation, the epicardial contour is slightly enlarged, hence, erosion is applied to shrink the outline. The result of the endocardial and epicardial contours are shown in Fig. 9(a).

For the basal end, the iteration stops with the refinement of the endocardium. In the apical direction, there is no endocardial contour anymore, as the endocardial iteration stops if the semi axis falls below a certain threshold θ_{r}. Therefore, the previously estimated epicardial contour is used for the refinement with decreasing radius. The epicardial refinement for the apex is stopped when the semi-axes of the epicardium falls below a threshold $\theta_{\mathrm{r}_{epi}}$.

3.5. Mesh generation

In the final step, the segmented endocardial and epicardial contours are extracted as 3-D surface meshes. For the mesh generation the marching cubes algorithm is used to obtain the iso-surfaces of the contours (Lorensen and Cline, 1987). The output of the algorithm is a triangular mesh consisting of a set of vertices and connected faces. The extracted vertices and faces, as well as face normals are then saved in the stl-file format. Fig. 9(b) depicts an example of such a mesh, where the endocardial surface is red, the epicardial surface is yellow and the scar is visualized in purple.
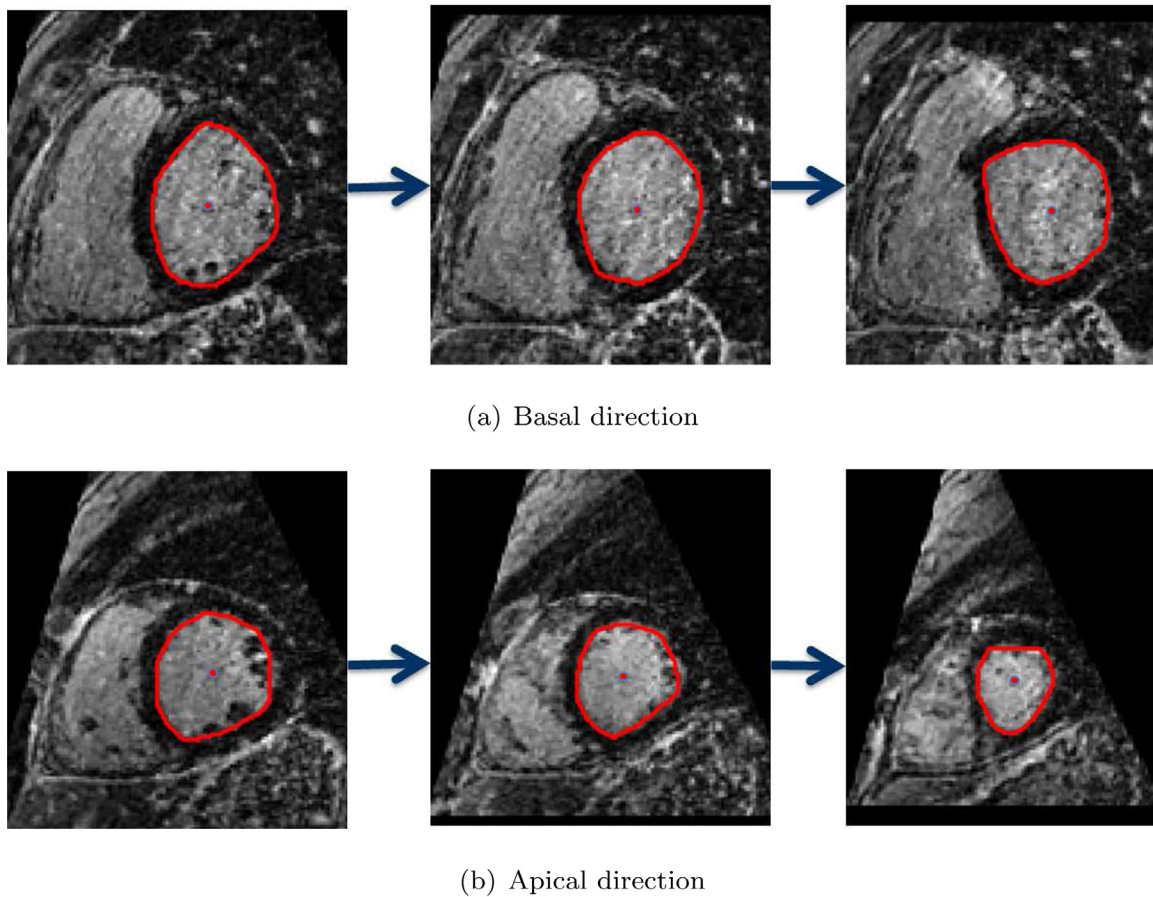
(a) Basal direction

(b) Apical direction

Fig. 7. (a) Refinement for the basal direction, considering the shape and center of the previous contours to guarantee for inter-slice smoothness. (b) Refinement for the apical direction considering the radius, shape and center of the previous contour to guarantee for inter-slice smoothness.
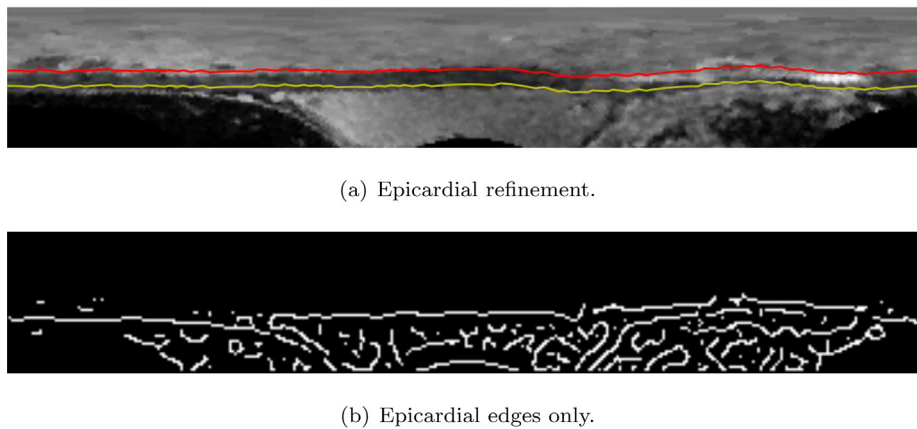

(a) Epicardial refinement.

(b) Epicardial edges only.

Fig. 8. (a) Final endocardial contour in red and enlarged epicardial contour in yellow. (b) Edge image, showing only the remaining edges after the exclusion of the endocardium. (For interpretation of the references to color in this figure legend, the reader is referred to the web version of this article.)

4. Evaluation and results

4.1. Data description

The automatic segmentation of the LV endocardium and epicardium was evaluated on 30 clinical MRI data sets from individual patients acquired at two clinical sites. The two clinical sites are distinguished in cohort 1 and cohort 2.

From the first clinical site, the data was acquired using a MAG-NETOM Skyra 3T scanner (Siemens Healthcare GmbH, Erlangen, Germany). The free-breathing whole heart 3-D LGE-MRI was performed based on a protocol adapted from Forman et al. (2014). The main difference is, that the sequence is inversion prepared. The patient specific TI time was adjusted with a TI scout scan prior to the 3-D LGE acquisition. For acceleration, the Cartesian variable-density spiral phyllotaxis sampling pattern was set up for a net acceleration of 7.7 relative to the fully sampled k-space. The acquisition utilizing a GRE sequence, had the following parameters: TR/TE 4.0/1.5 ms, radio frequency excitation angle $20°$, FOV 247–270 mm $\times$ 270 mm $\times$ 135–180 mm^3, voxel size 1.3 mm^3

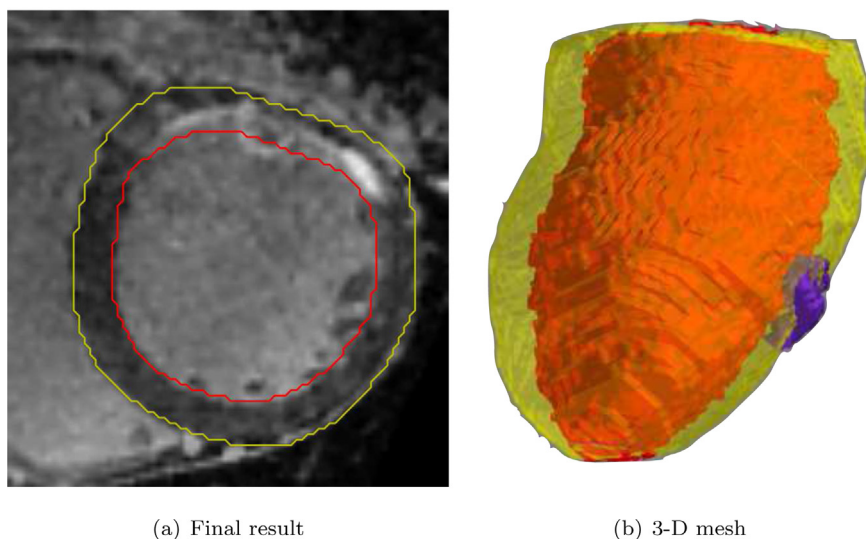(a) Final result   (b) 3-D mesh

Fig. 9. (a) Final result of the endo- and epicardial contour in Cartesian coordinates. (b) Final result in 3-D. The endocardial surface is visualized in red and the epicardial outline is visualized in yellow, with a myocardial infarction visualized in purple. (For interpretation of the references to color in this figure legend, the reader is referred to the web version of this article.)

isotropic and a receiver bandwidth of 401 Hz/Px. The acquisition window of the ECG-triggered sequence was adapted to the patient specific cardiac resting phase in mid-diastole. Image reconstruction was fully integrated on the scanner and performed with a regularized SENSE-type iterative reconstruction as described in (Liu et al., 2012). For all data sets, the regularization parameter was fixed to 0.002 and image reconstruction was terminated after 20 iterations of the mFISTA algorithm.

From the second clinical site, the data was acquired using two different clinical scanners, MAGNETOM Verio 3T and MAGNETOM Espree 1.5T (Siemens Healthcare GmbH, Erlangen, Germany). The acquisition utilizing a GRE sequence had the following parameters: TR/TE 2.76–4.02 ms/1.38–2.01 ms, radio frequency excitation angle 13–14°, FOV 379–384 × 379–384, voxel size $(0.66–0.85 \times 0.66–0.85 \times 1.5–1.7)$ mm^3 and a receiver bandwidth of 349–755 Hz/Px. Image reconstruction was performed using parallel imaging (Griswold et al., 2002).

Fig. 10 shows an example data set for each cohort, (a) and (c) shows the short axis view and (b) and (d) the long axis. In the second cohort no additional fat suppression was applied, which leads to various enhancements, especially in the apex, see Fig. 10(d). The different resolution of cohort 1 and 2 in the z-axis has no influence on the algorithm.

4.2. Evaluation

Gold standard annotations of the LV endo- and epicardium were provided by a physician as well as a clinical expert. The annotations were performed using Slicer (Fedorov et al., 2012) or Seg3D (CIBC, 2015). The observers were asked to segment the endocardial and epicardial contour separately.

For the segmentation of the endo- and epicardium several parameters hat to be chosen heuristically. A summary of all the parameters is provided in Table 1.

4.2.1. Metrics

Given the gold standard annotation, the segmentation was evaluated using two different measures. First, the **Dice coefficient (DC)** as a quantitative score of the segmentation quality is evaluated, as it measures the proportion of the true positives in the segmentation.

Table 1
Parameters for the left ventricle segmentation. These parameters were chosen heuristically.

Parameters for LV segmentation		
Description	Symbol	Value
Distance between contour points	θ_{dist}	4
Sub-sampling rate	ξ	4
Difference between areas	θ_{diff}	±25%
Difference between centers	θ_{C}	5
Base reached	$\theta_{b_{\max}}$	≥188%
Enlargement for epicard	θ_{epi}	6
Apex reached epicard	$\theta_{r_{epi}}$	<2

Dice scores ranges from 0 to 1, with 1 corresponding to a perfect overlap. The metric is defined as

$$DC(\mathcal{A}, \mathcal{B}) = \frac{2|\mathcal{A} \cap \mathcal{B}|}{|\mathcal{A}| + |\mathcal{B}|}, \tag{5}$$

where $\mathcal{A}$ is the segmentation result and $\mathcal{B}$ is the gold standard annotation. For the Dice coefficient the whole 3-D volume was considered.

The second evaluation method is the **average surface distance (ASD)** between the surface voxel of the binary mask $\mathcal{A}$ and their nearest surface voxel of binary object $\mathcal{B}$, averaged over all contour points and all slices of the volume.

4.2.2. Assessment

The two different measures were applied to the whole volume, differentiating the endo- and epicardium. Furthermore, the inter-observer variability between the observers was investigated. In addition, the volume was separated in three parts, base, mid-cavity and apex, by dividing the gold standard annotation into equal thirds, perpendicular to its long axis (Ma et al., 2012).

4.2.3. Smoothing

As the gold standard annotation was done in the sagittal, coronal and axial plane the results look frayed in the short axis orientation, see Fig. 11(a) for an example. To overcome this issue, the gold standard annotation was post-processed by applying the convex hull to the contour points for every slice in the short axis orientation. To be more precise, the convex hull was estimated in 2-D for each
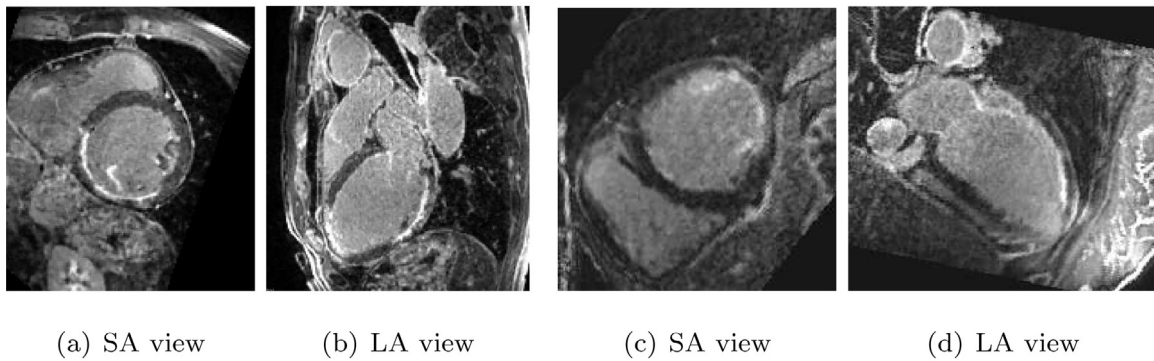
(a) SA view   (b) LA view   (c) SA view   (d) LA view

Fig. 10. (a) and (b) shows one example data set of the first cohort in a short and long axis orientation. (c) and (d) depicts an example data set of the second cohort. Here the voxel spacing is not isotropic and no additional fat suppression was applied. This results in further enhancements in the apical region of the left ventricle.
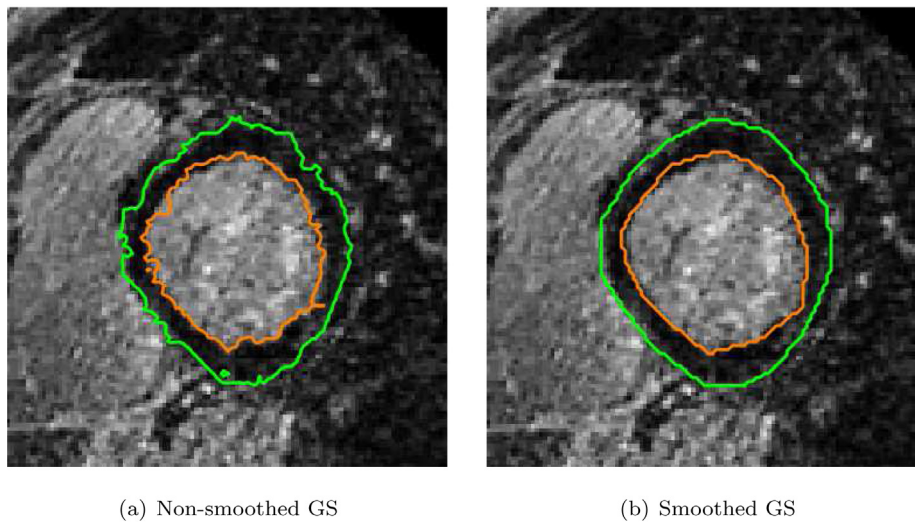

(a) Non-smoothed GS   (b) Smoothed GS

Fig. 11. (a) Example of the original non-smoothed (NS) gold standard (GS) annotation in the short axis orientation. It can be seen that the contours are very frayed. (b) Smoothed (S) gold standard annotation GS* after applying the convex hull to the contour points.

slice without considering the overall 3-D shape. An example of the smoothed contour is shown in Fig. 11(b).

4.2.4. Scar volume

As already mentioned, LGE-MRI is used to visualize regions of fibrosis and myocardial infarction in the myocardium. This information can be important for treatment planning and success prediction.

There exist already various of different methods that can be used for scar segmentation, e.g. threshold based methods with a fixed number of standard deviations from the mean intensity of the healthy myocardium, full-width-at-half-maximum approach or clustering methods (Karim et al., 2013, 2016; Rajchl et al., 2014). As the amount of scar tissue is an important information, however the scar tissue segmentation itself is out of scope of this journal, a simple but widely used threshold based approach was implemented to compare the difference in scar volume. The scar segmentation requires the prior delineation of the myocardium. From the myocardium, an intensity histogram is computed. It is expected, that the histogram is bi-modal in case of a myocardial infarction. One mode for the viable tissue and the other one for the enhanced scar tissue. The threshold θ_{mode} between the two modes is determined using Otsu's method (Otsu, 1979). The threshold of the scarring θ_{scar} is then defined as follows:

$$\theta_{scar} = \mu_l + 2 \cdot \sigma_l, \tag{6}$$

where μ_l is the mean intensity of the lower mode of the intensity histogram and σ_l the standard deviation of the lower mode. After the scar tissue is quantified the total scar volume compared to the volume of the myocardium can be computed. The scar volume is estimated for the two gold standard annotations as well as for the fully automatic segmentation approach.

4.3. Results

4.3.1. Gold standard annotation comparison

Fig. 12 compares the two different gold standard annotations obtained from the clinical experts, from base to apex. In the first row, the smoothed gold standard annotations from the endocardium are shown. In the second row, the smoothed gold standard annotations from the epicardium are shown. In this data set a huge myocardial scarring is present. It can be seen that the contours differ especially in the apex and at the left ventricular outflow tract. These regions also show the largest differences compared to the fully automatic segmentation.

In addition to the inter-observer variability, the DC and ASD between the smoothed gold standard annotation and non-smoothed annotations was evaluated. The endocard had a mean DC of 0.96 ± 0.01. The best segmentation overlap had a Dice of 0.97 and the worst a DC of 0.89. The epicard had a mean DC of 0.96 ± 0.02. The best match yielded a DC of 0.98 and the worst a DC of 0.92. Using the average surface distance, the endocard had a
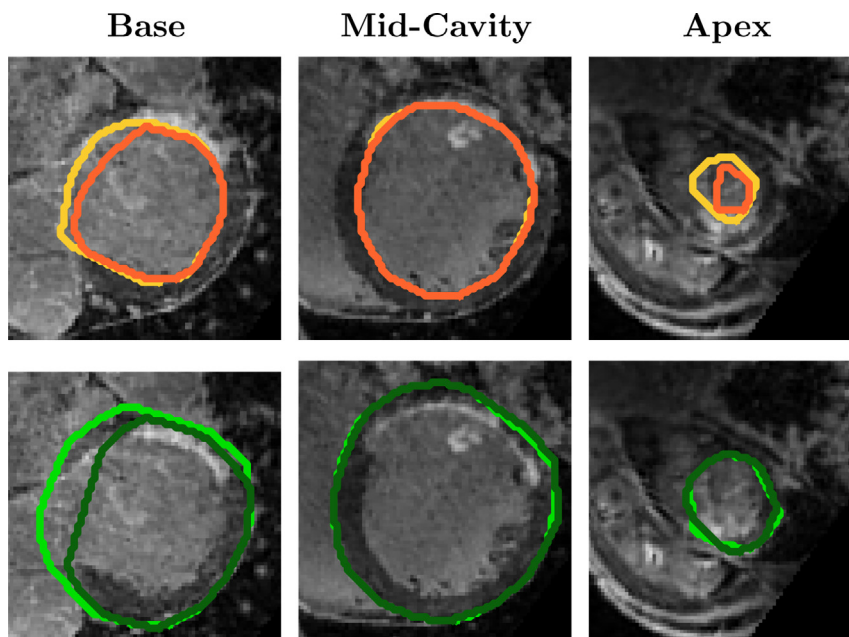
Fig. 12. Comparison of the segmentation result for the two observers. The first row depicts the smoothed gold standard annotation from the endocardium, where the lighter orange contour is from the physician and the darker contour from the clinical expert. The second row shows the smoothed gold standard annotation of the epicardium, where the light green contour is from the physician and the dark green from the clinical expert. (For interpretation of the references to color in this figure legend, the reader is referred to the web version of this article.)

Table 2
Comparison of the smoothed gold standard annotation to the non-smoothed gold standard annotation, using the Dice coefficient (Dice) and the average surface distance (ASD). The results are shown separately for the endocardial (Endo), epicardial (Epi) contour.

Smoothing effect		
Description	Dice	ASD (mm)
Endo	0.96 ± 0.01	0.68 ± 0.32
Epi	0.96 ± 0.02	0.79 ± 0.40

mean distance of 0.68 mm ± 0.32 mm, with a minimum of 0.36 mm and a maximum of 2.41 mm. For the epicard a mean distance of 0.79 mm ± 0.40 mm was evaluated, with a minimum of 0.33 mm and a maximum distance of 1.92 mm. The results for the smoothing impact are summarized in Table 2. As the smoothing has no big influence for the Dice coefficient as shown in Table 2 and the results seem more physiologically meaningful compared to the non-smoothed results as seen in Fig. 11, only the smoothed gold standard annotation is considered for the further evaluation.

4.3.2. Dice coefficient

For the **smoothed gold standard** a DC of 0.84 ± 0.04 was achieved. The best segmentation result had a DC of 0.91 and the worst a DC of 0.72. For the epicard, an overall DC of 0.80 ± 0.06 was achieved. The best segmentation of the epicardium yielded a DC of 0.91 and the worst a DC of 0.68. The inter-observer variability of the post-processed data resulted in a DC of 0.92 ± 0.04. In Table 3 a distinction between the two different clinical cohorts is made. It can be seen that the results for the endocardial contour extraction are similar with a Dice coefficient of around 0.84. However, the DC for the epicard is worse for the second cohort, with a mean of 0.78.

Furthermore, the Dice coefficient of the basal, mid-cavity and apex was evaluated separately considering the endocardium and the epicardium together regarding the smoothed gold standard annotation. The algorithm performs best for the mid-cavity area, where a DC of 0.86 ± 0.05 was achieved. The error is larger for the
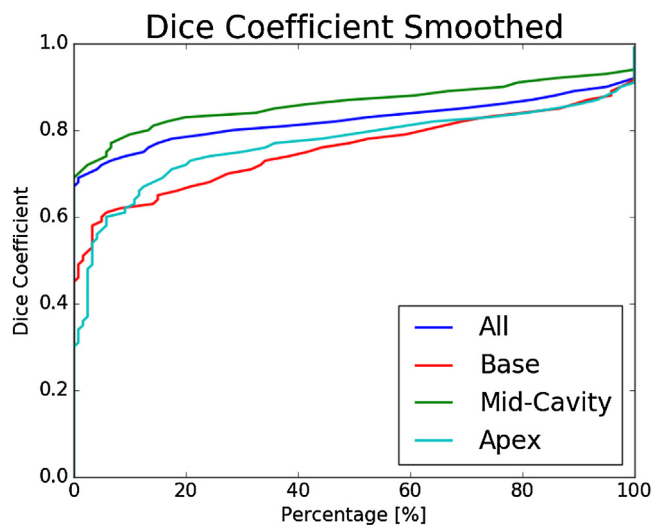

Fig. 13. Considering the endocardium and epicardium together, an average Dice coefficient of 0.82 ± 0.05 was achieved. Furthermore, the LV was divided into three parts, base, mid-cavity and apex. For the basal region a DC of 0.75 ± 0.09 was achieved, for the mid-cavity a DC of 0.86 ± 0.05 and for the apex a DC of 0.77 ± 0.10.

basal area and the apex, where a DC of 0.75 ± 0.09 and 0.77 ± 0.10 was achieved. This is visualized in Fig. 13.

4.3.3. Average surface distance

For the **smoothed gold standard annotation**, the endocard had a mean distance of 2.75 ± 0.73 in mm, with a minimum of 1.49 mm, and a maximum of 4.48 mm. The epicard had a mean distance of 4.29 ± 1.18, with a minimum average of 1.90 mm, and a maximum average of 6.72 mm. The inter-observer variability between the two observers resulted in a mean ASD of 1.35 ± 0.73 mm. In Table 4 there is a distinction for the two different clinical cohorts. Here, the same observations can be seen as for the Dice coefficient.

Table 3
Quantitative results of LV segmentation, using the Dice coefficient and the smoothed gold standard annotation. The results are shown separately for the endocardial (Endo) and epicardial (Epi) contour. Furthermore, it is distinguished between the two different clinical cohorts.

Dice coefficient for smoothed annotations					
Description		Mean	Observer 1	Observer 2	Observer overlap
Cohort 1	Endo	0.85 ± 0.06	0.84 ± 0.06	0.85 ± 0.06	0.96 ± 0.02
	Epi	0.85 ± 0.06	0.83 ± 0.06	0.86 ± 0.06	0.94 ± 0.02
Cohort 2	Endo	0.84 ± 0.03	0.83 ± 0.03	0.84 ± 0.03	0.91 ± 0.04
	Epi	0.78 ± 0.04	0.78 ± 0.04	0.78 ± 0.05	0.87 ± 0.05

Table 4
Quantitative results of LV segmentation, using the average surface distance in mm and the smoothed gold standard annotation. The results are shown separately for the endocardial (Endo) and epicardial (Epi) contour. Where observer 1 corresponds to the physician and observer 2 to the clinical expert.

Average surface distance for smoothed annotations in mm					
Description		Mean	Observer 1	Observer 2	Observer overlap
Cohort 1	Endo	2.65 ± 0.96	2.73 ± 0.90	2.58 ± 1.06	0.83 ± 0.50
	Epi	3.42 ± 1.20	3.72 ± 1.22	3.13 ± 1.17	1.42 ± 0.51
Cohort 2	Endo	2.79 ± 0.61	2.88 ± 0.60	2.70 ± 0.63	1.57 ± 0.71
	Epi	4.65 ± 0.96	4.90 ± 0.80	4.41 ± 1.06	2.97 ± 1.19

4.3.4. Qualitative results

Fig. 14 shows an example for a qualitative evaluation for one clinical data set of the first cohort. The first row shows the pseudo SA slices from basal to apical direction without any contours. The second row depicts the gold standard annotation without smoothing from the physician, where the endocardium is marked in orange and the epicardium in green. The third row illustrates the gold standard annotation with smoothing, where the endocardium is marked in orange and the epicardium in green. The fourth row delineates the final result of the presented segmentation algorithm, where the endocardial contour is red and the epicardial contour is yellow. It can be seen that the presented result matches well with the smoothed gold standard annotation. However, the manual annotation looks frayed. Furthermore, it can be observed that the biggest variance of the annotations is in the apex, which is also shown in Fig. 13, regarding the DC.

4.3.5. Scar volume results

The myocardial scar volume was evaluated for the segmentation result as well as for the two gold standard annotations. The measure is in percentage compared to the total myocardial volume. The scar volume evaluation shows that all the 3-D LGE MRI scans contain scar. Fig. 15 compares the percentage of scar volume for all 30 data sets.

4.3.6. Parameter sensitivity

As many parameters were set, as shown in Table 1, the sensitivity of these parameters was evaluated, see Fig. 16. It can be seen that sensitivity of the parameters is low and the mean value is always in the same range.

5. Discussion

The runtime is an important factor for the employment in clinical practice. The current implementation is single threaded only, without any optimization. The evaluation was performed on an Intel i7 with 2.80 GHz equipped with 16 GB RAM. The whole segmentation pipeline needs less than 5 minutes, implemented with Python. The proposed method achieved a Dice coefficient of 0.84 ± 0.04 for the endocardium and 0.80 ± 0.06 for the epicardium. The results for the base and the apical regions are worse compared to the mid-cavity. For the base, this can be attributed to the fact that the transition from the LV to the outflow tract is smooth. Therefore, the slice where the segmentation algorithm stops is not defined by

the volumetric data set, compared to regular 2-D LGE-MRI. Furthermore, the clinical experts annotated the data in the axial, sagittal and coronal planes, so the transition of the outflow tract is even harder to delineate. In the apex the endocardium gets very small. If there is a myocardial infarction it is even harder to delineate between myocardium and blood pool, especially if the annotation is not done in the short axis orientation. This is another reason, for the reduced Dice coefficient in the apical region. Furthermore, for the data of the second cohort, no additional fat suppression was applied, therefore various enhancements in the apex appeared. The last two columns of Fig. 14 depict the apical region without scar, however it can be seen that there the biggest differences occur compared to the gold standard annotation.

Approaches as presented in Peters et al. (2007) or Zhuang et al. (2010) are not suitable for our case. First of all the two data sets differ. Furthermore, the optimization of such models is difficult as there is no clear boundary between the myocardial infarction and the blood pool. Therefore, no model based approach was applied. To improve the results for the base, a cutoff parameter could be defined to make an identical decision for the outflow tract. Furthermore, it can be seen that the results for the epicardium segmentation of cohort two is worse compared to cohort one. This can be explained by the insufficient fat suppression of the MRI data.

A comparison across different studies is difficult to perform, as data sets differ. Also, all work was performed on 2-D LGE-MRI, but the focus of this study was on 3-D LGE-MRI only. Nevertheless, the proposed algorithm achieves similar or better results, in particular when compared with the results by Albà et al. (2014). They reported a Dice coefficient of 0.81 ± 0.05, solely using 2-D LGE-MRI. In the following the advantages of the presented approach compared to the reported methods are identified.

First, Dikici et al. (2004) and Wei et al. (2011) only consider the 2-D slices without taking the longitudinal axis into account. This can lead to inter-slice shifts and to discontinuous 3-D shapes. In comparison, in this work the center, radius and shape of the previously found slices are considered, which allows for an inter-slice smoothness.

Second, Ciofolo et al. (2008) used a 3-D deformable mesh for the LV segmentation, where the meshes were only attracted to features in the SA slices. As there were no features considered in the other slices, this approach can lead to inter-slice shifts. Wei et al. (2013), who also deformed 3-D meshes, worked in a 3-D framework and considered the long axis of the image. This approach added more features for the deformation and resulted in a smoother
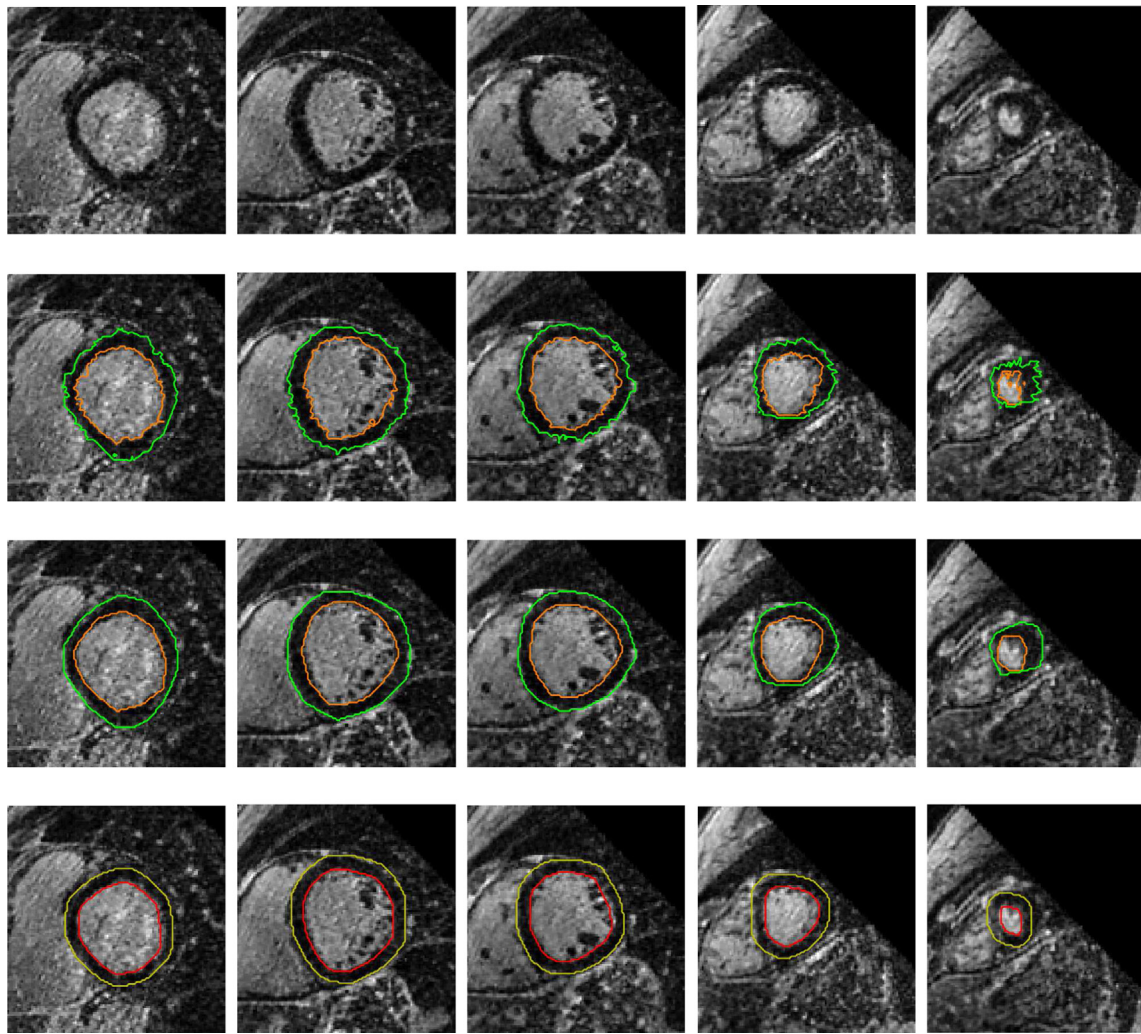
Fig. 14. Comparison of the segmentation result for one data set. The first row shows the pseudo SA slices from basal to apical direction without any contours. The second row depicts the gold standard annotation from the physician without smoothing, where the endocardium is marked in orange and the epicardium in green. The third row depicts the smoothed gold standard annotation, where the endocardium is marked in orange and the epicardium in green. The fourth row delineates the final result of the presented segmentation algorithm, where the endocardial contour is red and the epicardial contour is yellow. (For interpretation of the references to colour in this figure legend, the reader is referred to the web version of this article.)

shape. Our method, while computational simple, uses the pseudo SA slice and considers the propagation in the succeeding slices to deal with potential misalignment and avoid segmentation errors, without the need to segment any long axis or CINE images.

Although the gold standard annotation was obtained from a physician and a clinical expert, it still involves inaccuracies regarding the manual delineation of the myocardium. To some extent, this is due to a lack of good annotation tools. This issue is also confirmed by the larger inter-observer variability. We have tried to compensate this by an additional smoothing of the gold standard annotations. The effect of the smoothing is rather minimal, as shown in Table 2. The Dice coefficient changes only about 0.04 and the ASD is not notably affected (less than 1 mm). It has to be noted that the smoothing is only in the pseudo-short-axis slices and therefore, does not consider the 3-D shape of the ventricle. Hence, this can lead to some stepping artifacts. Furthermore we could not compare our segmentation results to previous methods as stated in Section 2, as there is none available for 3-D LGE-MRI.

For the precise scar quantification, a prerequisite is the accurate and reliable segmentation of the left ventricle. However, the scar quantification heavily depends on the technique applied (Karim et al., 2016; Rajchl et al., 2014). We investigated the scar volume,

by applying a simple threshold based approach. The evaluation showed, that all 30 data sets contain myocardial scarring. And that the algorithm is able to segment regions of myocardial scarring properly. Having the segmentation of the scar, the myocardial infarction itself can be analyzed further. For example the infarct size and mass can be estimated. As the total scar burden is a good predictor for the success of a therapy. In addition to that, the type of scarring is of interest. In clinical practice, three types of fibrosis are differentiated: endocardial, epicardial and transmural scar. Having the segmentation of the endocardium and epicardium the transmurality of the scar can be classified precisely (Reiml et al., 2016).

The benefit of the presented method is the independence of any user input. The algorithm requires only the 3-D LGE-MRI volume. This results in a more robust segmentation. However, a graphical user interface is provided in case the user is not satisfied with the segmentation result and the contours can be edited manually.

6. Conclusion

The purpose of this study was to provide an automatic, accurate, and stable left ventricle myocardial segmentation method for
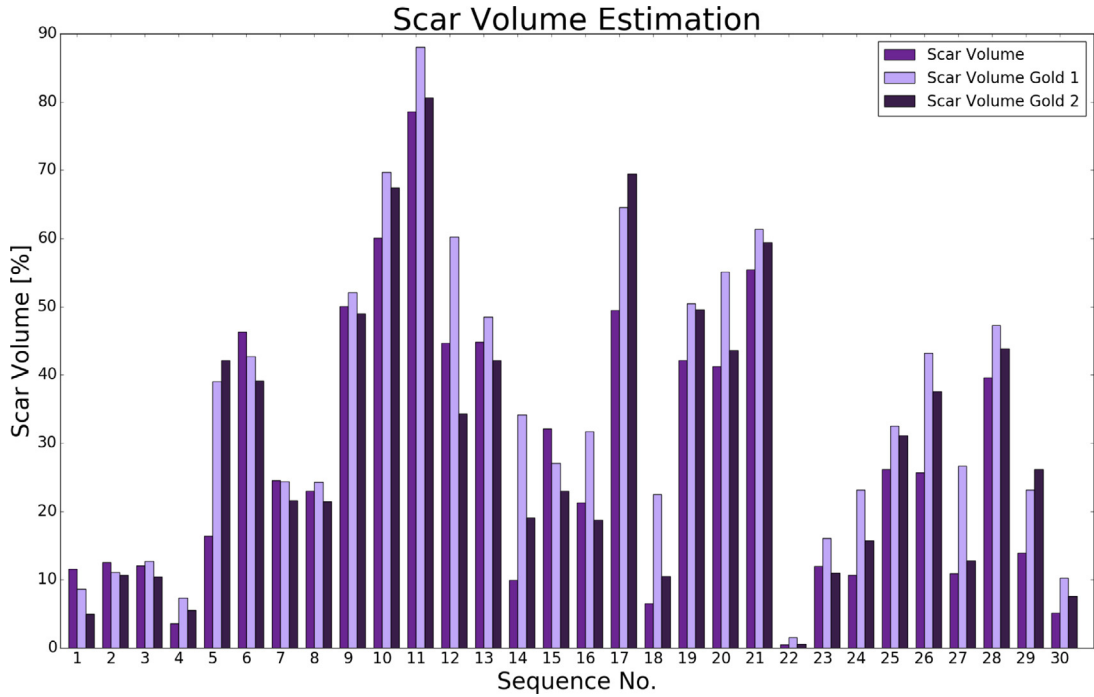
Fig. 15. Comparison of the scar volume in percentage for all 30 cases, considering the segmentation result and the two gold standard annotations.
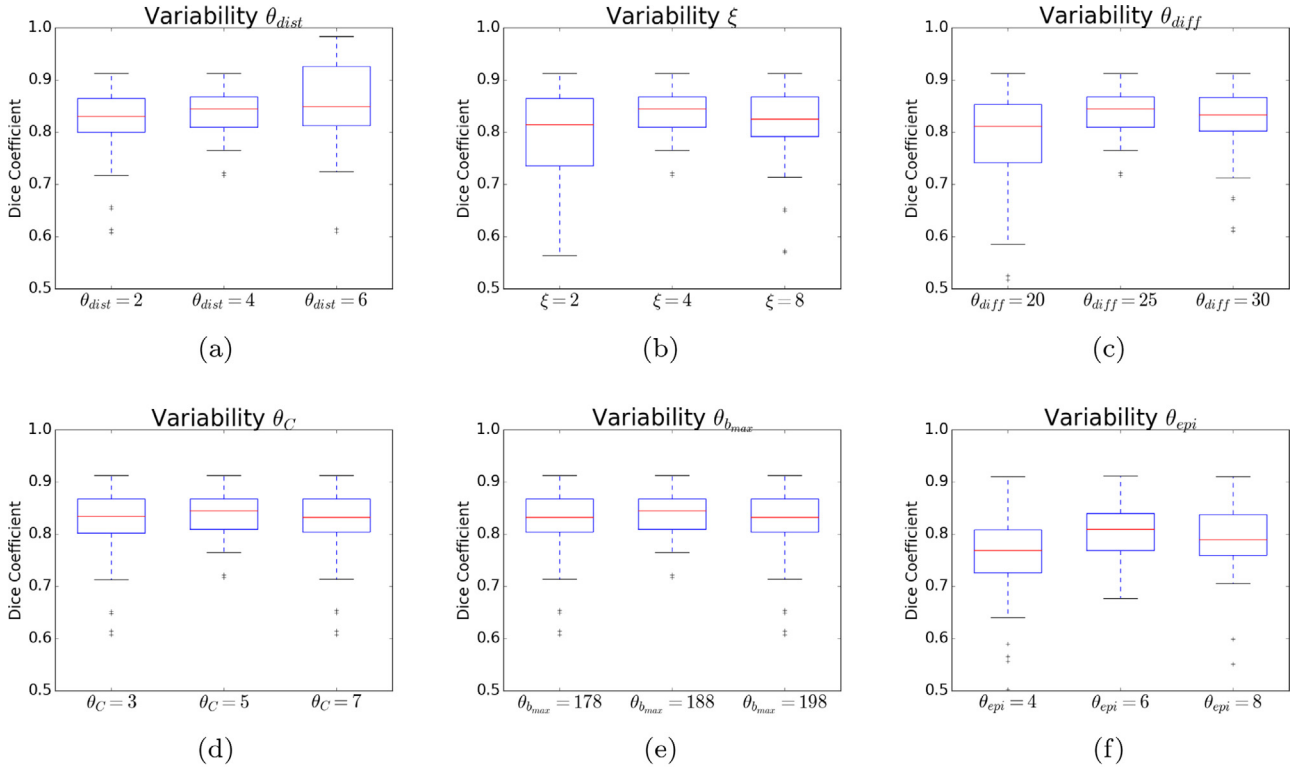

Fig. 16. Parameter variability evaluation. (a) Variability evaluation of the distance between points θ_{dist}. (b) Variability evaluation of the sub-sampling rate ξ. (c) Variability evaluation of the distance between areas θ_{diff}. (d) Variability evaluation of the distance between centers θ_C. (e) Variability evaluation of base threshold $\theta_{b_{\max}}$. (f) Variability evaluation of the enlargement of the epicard θ_{epi}.

3-D LGE-MRI sequences. Segmentation of the LV endo- and epicardium has been studied in literature, but only a few methods focused solely on LGE-MRI data. None of them consider 3-D LGE-MRI, based on our knowledge. The presented work solely uses 3-D LGE-MRI for the segmentation, unlike most related work, which make use of CINE MRI for the LGE-MRI segmentation.

Future work includes the investigation of scar quantification methods and an application of the presented algorithms to other segmentation tasks, such as the right ventricle. In the course of this work, an automatic segmentation method for the left ventricle endo- and epicardium has been presented that provides accurate and consistent results for 3-D LGE-MRI. Our method achieved an

overall Dice coefficient of 0.84 for the endocard and 0.80 for the epicardium. Using the average surface distance the endocard had a mean error of 2.75 mm and the epicard had a mean error of 4.29 mm. However, the scar quantification depends on the technique applied (Rajchl et al., 2014) and also on the preferences of the physician. Therefore, we did not focus on a new scar quantification approach in this work. A clear benefit of the presented method is the independence from an anatomical scan and from user interaction.

Disclaimer

The methods and information presented in this paper are based on research and are not commercially available.

Conflict of interest

C. Forman, M. Schmidt and A. Brost are employed by Siemens Healthcare GmbH. C. Tillmanns and A. Maier have received research funding from Siemens Healthcare GmbH.

Acknowledgments

References

Albà, X., i Ventura, F., Rosa, M., Lekadir, K., Tobon-Gomez, C., Hoogendoorn, C., Frangi, A.F., 2014. Automatic cardiac LV segmentation in MRI using modified graph cuts with smoothness and interslice constraints. Magn. Reson. Med. 72 (6), 1775–1784, http://dx.doi.org/10.1002/mrm.25079.

Azancot, A., Caudell, T., Allen, H., Horowitz, S., Sahn, D., Stoll, C., Thies, C., Valdes-Cruz, L., Goldberg, S., 1983. Analysis of ventricular shape by echocardiography in normal fetuses, newborns, and infants. Circulation 68 (6), 1201–1211, http://dx.doi.org/10.1161/01.CIR.68.6.1201.

Bilchick, K., Dimaano, V., Wu, K., Helm, R., Weiss, R., Lima, J., Berger, R., Tomaselli, G., Bluemke, D., Halperin, H., Abraham, T., Kass, D., Lardo, A., 2008. Cardiac magnetic resonance assessment of dyssynchrony and myocardial scar predicts function class improvement following cardiac resynchronization therapy. JACC: Cardiovasc. Imaging 1 (5), 561–568, http://dx.doi.org/10.1016/j.jcmg.2008.04.013.

Börnert, P., Jensen, D., 1995. Coronary artery imaging at 0.5 T using segmented 3D echo planar imaging. Magn. Reson. Med. 34 (6), 779–785, http://dx.doi.org/10.1002/mrm.1910340602.

Canny, J., 1986. A computational approach to edge detection. IEEE Trans. Pattern Anal. Mach. Intell. 8 (6), 679–698, http://dx.doi.org/10.1109/TPAMI.1986.4767851.

CIBC, 2015. Seg3D: Volumetric Image Segmentation and Visualization. Scientific Computing and Imaging Institute (SCI), Download from: http://www.seg3d.org.

Ciofolo, C., Fradkin, M., 2008. Segmentation of pathologic hearts in long-axis late-enhancement MRI. In: Medical Image Computing and Computer-Assisted Intervention-MICCAI 2008. Springer, pp. 186–193, http://dx.doi.org/10.1007/978-3-540-85988-8_23.

Ciofolo, C., Fradkin, M., Mory, B., Hautvast, G., Breeuwer, M., 2008. Automatic myocardium segmentation in late-enhancement MRI. In: 5th IEEE International Symposium on Biomedical Imaging: From Nano to Macro, 2008, ISBI 2008. IEEE, pp. 225–228, http://dx.doi.org/10.1109/ISBI.2008.4540973.

Dickstein, K., Bogale, N., Priori, S., Auricchio, A., Cleland, J.G., Gitt, A., Limbourg, T., Linde, C., van Veldhuisen, D.J., Brugada, J., et al., 2009. The European cardiac resynchronization therapy survey. Eur. Heart J. 30 (20), 2450–2460, http://dx.doi.org/10.1093/eurheartj/ehp359.

Dijkstra, E., 1959. A note on two problems in connexion with graphs. Numer. Math. 1 (1), 269–271, http://dx.doi.org/10.1007/BF01386390.

Dikici, E., ODonnell, T., Setser, R., White, R., 2004. Quantification of delayed enhancement MR images. In: Medical Image Computing and Computer-Assisted Intervention-MICCAI 2004. Springer, pp. 250–257, http://dx.doi.org/10.1007/978-3-540-30135-6_31.

Duann, J.R., Chiang, S.H., Lin, S.B., Lin, C.C., Chen, J.H., Su, J.L., 1999. Assessment of left ventricular cardiac shape by the use of volumetric curvature analysis from 3D echocardiography. Comput. Med. Imaging Graph. 23 (2), 89–101, http://dx.doi.org/10.1016/S0895-6111(98)00065-2.

Fedorov, A., Beichel, R., Kalpathy-Cramer, J., Finet, J., Fillion-Robin, J.C., Pujol, S., Bauer, C., Jennings, D., Fennessy, F., Sonka, M., et al., 2012. 3D Slicer as an image

computing platform for the quantitative imaging network. Magn. Reson. Imaging 30 (9), 1323–1341, http://dx.doi.org/10.1016/j.mri.2012.05.001.

Forman, C., Piccini, D., Grimm, R., Hutter, J., Hornegger, J., Zenge, M., 2014. High-resolution 3D whole-heart coronary MRA: a study on the combination of data acquisition in multiple breath-holds and 1D residual respiratory motion compensation. Magn. Reson. Mater. Phys. Biol. Med. 27 (5), 435–443, http://dx.doi.org/10.1007/s10334-013-0428-x.

Frangi, A.F., Niessen, W.J., Viergever, M.A., 2001. Three-dimensional modeling for functional analysis of cardiac images: a review. IEEE Trans. Med. Imaging 20 (1), 2–5, http://dx.doi.org/10.1109/42.906421.

Griswold, M.A., Jakob, P.M., Heidemann, R.M., Nittka, M., Jellus, V., Wang, J., Kiefer, B., Haase, A., 2002. Generalized autocalibrating partially parallel acquisitions (GRAPPA). Magn. Reson. Med. 47 (6), 1202–1210, http://dx.doi.org/10.1002/mrm.10171.

Jolliffe, I., 2002. Principal Component Analysis. Wiley Online Library, http://dx.doi.org/10.1002/9781118445112.stat06472.

Karim, R., Bhagirath, P., Claus, P., Housden, R.J., Chen, Z., Karimaghaloo, Z., Sohn, H.M., Rodríguez, L.L., Vera, S., Albà, X., et al., 2016. Evaluation of state-of-the-art segmentation algorithms for left ventricle infarct from late gadolinium enhancement MR images. Med. Image Anal. 30, 95–107, http://dx.doi.org/10.1016/j.media.2016.01.004.

Karim, R., Housden, J., Balasubramaniam, M., Chen, Z., Perry, D., Uddin, A., Al-Beyatti, Y., Palkhi, E., Acheampong, P., Obom, S., et al., 2013. Evaluation of current algorithms for segmentation of scar tissue from late gadolinium enhancement cardiovascular magnetic resonance of the left atrium: an open-access grand challenge. J. Cardiovasc. Magn. Reson. 15 (1), 1–17, http://dx.doi.org/10.1186/1532-429X-15-105.

Kellman, P., Arai, A., 2012. Cardiac imaging techniques for physicians: late enhancement. J. Magn. Reson. Imaging 36 (3), 529–542, http://dx.doi.org/10.1002/jmri.23605.

Klein, S., Staring, M., Murphy, K., Viergever, M.A., Pluim, J.P., 2010. Elastix: a toolbox for intensity-based medical image registration. IEEE Trans. Med. Imaging 29 (1), 196–205, http://dx.doi.org/10.1109/TMI.2009.2035616.

Kurzendorfer, T., Brost, A., Forman, C., Schmidt, M., Tillmanns, C., Hornegger, J., 2015. Semi-automatic segmentation and scar quantification of the left ventricle in 3-D late gadolinium enhanced MRI. In: ESMRMB (Ed.), 32nd Annual Scientific Meeting of the ESMRMB. , pp. 318–319, http://dx.doi.org/10.1007/s10334-015-0489-0.

Liu, J., Rapin, J., Chang, T.c., Schmidt, P., Bi, X., Lefebvre, A., Zenge, M., Mueller, E., Nadar, M., 2012. Regularized reconstruction using redundant Haar wavelets: a means to achieve high under-sampling factors in non-contrast-enhanced 4D MRA. In: Proc. ISMRM, vol. 178.

Lorensen, W., Cline, H., 1987. Marching cubes: a high resolution 3D surface construction algorithm. ACM Siggraph Comput. Graph. 21, 163–169, http://dx.doi.org/10.1145/37401.37422.

Ma, Y.L., Shetty, A.K., Duckett, S., Etyngier, P., Gijsbers, G., Bullens, R., Schaeffter, T., Razavi, R., Rinaldi, C.A., Rhode, K.S., 2012. An integrated platform for image-guided cardiac resynchronization therapy. Phys. Med. Biol. 57 (10), 2953, http://dx.doi.org/10.1088/0031-9155/57/10/2953.

McLeod, K., Saberniak, J., Haugaa, K., 2015. Statistical analysis of ventricular shape of ARVC patients and correlation with clinical diagnostic indices. J. Cardiovasc. Magn. Reson. 17 (Suppl. 1), P283, http://dx.doi.org/10.1186/1532-429X-17-S1-P283.

McMurray, J.J., Adamopoulos, S., Anker, S.D., Auricchio, A., Böhm, M., Dickstein, K., Falk, V., Filippatos, G., Fonseca, C., Gomez-Sanchez, M.A., et al., 2012. ESC guidelines for the diagnosis and treatment of acute and chronic heart failure 2012. Eur. J. Heart Fail. 14 (8), 803–869, http://dx.doi.org/10.1093/eurjhf/hfs105.

Otsu, N., 1979. A threshold selection method from gray-level histograms. Automatica 11 (285–296), 23–27.

Peters, J., Ecabert, O., Meyer, C., Schramm, H., Kneser, R., Groth, A., Weese, J., 2007. Automatic whole heart segmentation in static magnetic resonance image volumes. In: International Conference on Medical Image Computing and Computer-Assisted Intervention. Springer, pp. 402–410, http://dx.doi.org/10.1007/978-3-540-75759-7_49.

Petitjean, C., Dacher, J.N., 2011. A review of segmentation methods in short axis cardiac MR images. Med. Image Anal. 15 (2), 169–184.

Ponikowski, P., Anker, S.D., AlHabib, K.F., Cowie, M.R., Force, T.L., Hu, S., Jaarsma, T., Krum, H., Rastogi, V., Rohde, L.E., et al., 2014. Heart failure: preventing disease and death worldwide. ESC Heart Fail. 1 (1), 4–25, http://dx.doi.org/10.1002/ehf2.12005.

Rajchl, M., Stirrat, J., Goubran, M., Yu, J., Scholl, D., Peters, T.M., White, J.A., 2014. Comparison of semi-automated scar quantification techniques using high-resolution, 3-dimensional late-gadolinium-enhancement magnetic resonance imaging. Int. J. Cardiovasc. Imaging 31 (2), 349–357, http://dx.doi.org/10.1007/s10554-014-0553-2.

Rashid, S., Rapacchi, S., Shivkumar, K., Plotnik, A., Finn, P., Hu, P., 2015. Modified wideband 3D late gadolinium enhancement (LGE) MRI for patients with implantable cardiac devices. J. Cardiovasc. Magn. Reson. 17 (Suppl. 1), Q26, http://dx.doi.org/10.1186/1532-429X-17-S1-Q26.

Reiml, S., Toth, D., Panayiotou, M., Fahn, B., Karim, R., Behar, J.M., Rinaldi, C.A., Razavi, R., Rhode, K.S., Brost, A., et al., 2016. Interactive visualization for scar transmurality in cardiac resynchronization therapy. In: SPIE Medical Imaging. International Society for Optics and Photonics, http://dx.doi.org/10.1117/12.2214737, 97862S–97862S.

Rueckert, D., Sonoda, L.I., Hayes, C., Hill, D.L., Leach, M.O., Hawkes, D.J., 1999. Nonrigid registration using free-form deformations: application to breast MR images. IEEE Trans. Med. Imaging 18 (8), 712–721, http://dx.doi.org/10.1109/42.796284.

Shea, J.B., Sweeney, M.O., 2003. Cardiac resynchronization therapy a patient's guide. Circulation 108 (9), e64–e66, http://dx.doi.org/10.1161/01.CIR.0000085657.09097.38.

Shin, T., Lustig, M., Nishimura, D., Hu, B., 2014. Rapid single-breath-hold 3D late gadolinium enhancement cardiac MRI using a stack-of-spirals acquisition. J. Magn. Reson. Imaging 40 (6), 1496–1502, http://dx.doi.org/10.1002/jmri.24494.

Suinesiaputra, A., Cowan, B.R., Al-Agamy, A.O., Elattar, M.A., Ayache, N., Fahmy, A.S., Khalifa, A.M., Medrano-Gracia, P., Jolly, M.P., Kadish, A.H., et al., 2014. A collaborative resource to build consensus for automated left ventricular segmentation of cardiac MR images. Med. Image Anal. 18 (1), 50–62, http://dx.doi.org/10.1016/j.media.2013.09.001.

Tao, Q., Piers, S., Lamb, H., van der Geest, R., 2015. Automated left ventricle segmentation in late gadolinium-enhanced MRI for objective myocardial scar assessment. J. Magn. Reson. Imaging 42 (2), 390–399, http://dx.doi.org/10.1002/jmri.24804.

Thévenaz, P., Bierlaire, M., Unser, M., 2008. Halt on sampling for image registration based on mutual information. Sampl. Theory Signal Image Process. 7 (2).

Unberath, M., Maier, A., Fleischmann, D., Hornegger, J., Fahrig, R., 2015. Comparative evaluation of two registration-based segmentation algorithms: application to whole heart segmentation in CT. In: Leonhardt, S. (Ed.), Proceedings of the GRC. , pp. 5–8.

Wei, D., Sun, Y., Chai, P., Low, A., Ong, S.H., 2011. Myocardial segmentation of late gadolinium enhanced MR images by propagation of contours from cine MR images. In: Medical Image Computing and Computer-Assisted Intervention-MICCAI 2011. Springer, pp. 428–435, http://dx.doi.org/10.1007/978-3-642-23626-6_53.

Wei, D., Sun, Y., Ong, S.H., Chai, P., Teo, L., Low, A., 2013. Three-dimensional segmentation of the left ventricle in late gadolinium enhanced MR images of chronic infarction combining long-and short-axis information. Med. Image Anal. 17 (6), 685–697, http://dx.doi.org/10.1016/j.media.2013.03.001.

Zhuang, X., Rhode, K.S., Razavi, R.S., Hawkes, D.J., Ourselin, S., 2010. A registration-based propagation framework for automatic whole heart segmentation of cardiac MRI. IEEE Trans. Med. Imaging 29 (9), 1612–1625, http://dx.doi.org/10.1109/TMI.2010.2047112.